JOURNAL OF AIRCRAFT
Vol. 48, No. 3, May–June 2011

1303 Unmanned Combat Air Vehicle Flowfield Simulations and Comparison with Experimental Data

Scott E. Sherer,* Miguel R. Visbal,† and Raymond E. Gordnier‡
U.S. Air Force Research Laboratory, Wright-Patterson Air Force Base, Ohio 45433
and
Turgut O. Yilmaz§ and Donald O. Rockwell¶
Lehigh University Bethlehem, Pennsylvania 18015

DOI: 10.2514/1.C031195

In this work, high-order computations of the flowfield around a 1303 unmanned combat air vehicle configuration are performed and compared with recently collected experimental data obtained at Lehigh University. The computational approach used a high-order overset-grid flow solver developed in the Air Vehicles Directorate of the U.S. Air Force Research Laboratory that employs up-to-sixth-order compact finite differences and high-order, low-pass numerical filters to accurately resolve detailed flow features in a robust manner. The experimental data was collected via a particle image velocimetry technique in a free-surface water channel. Both quantitative and qualitative comparisons between computational and experimental results are done at a plane located at eight-tenths of the half-span for various Reynolds numbers and angles of attack, with the results comparing quite favorably for most flow conditions. Computational images of the flowfield are used to elucidate angle of attack and Reynolds number effects on this configuration, as well as to investigate the formation and evolution of the leading-edge and centerbody vortical structures and the impact that angle of attack has on their formation mechanisms.

Nomenclature

a, b	=	explicit compact differencing coefficients
C_{root}	=	wing root chord
C^*	=	local wing chord at given spanwise location
E_t	=	total specific energy
$\boldsymbol{F}$, $\boldsymbol{G}$, $\boldsymbol{H}$	=	inviscid vector fluxes
$\boldsymbol{F}_v$, $\boldsymbol{G}_v$, $\boldsymbol{H}_v$	=	viscous vector fluxes
f_i	=	explicit compact filter coefficients
$\boldsymbol{I}$	=	identity matrix
I_p, J_p, K_p	=	computational indices of interpolation donor point
$\mathcal{J}$	=	Jacobian of the coordinate transformation
L_{mac}	=	mean aerodynamic chord
L_{ref}	=	reference length ($L_{\text{ref}} = L_{\text{mac}}$)
M	=	Mach number
Pr	=	Prandtl number, 0.72 for air
p	=	nondimensional static pressure
$\boldsymbol{Q}$	=	vector of dependent variables
Re	=	reference Reynolds number, $\rho_\infty u_\infty L_{\text{ref}}/\mu_\infty$
$Re_{C_{\text{root}}}$	=	reference Reynolds number based on wing root chord, $\rho_\infty u_\infty C_{\text{root}}/\mu_\infty$
Re_{mac}	=	reference Reynolds number based on mean aerodynamic chord, $\rho_\infty u_\infty L_{\text{mac}}/\mu_\infty$
R^ξ, R^η, R^ζ	=	Laplace interpolation coefficients in ξ, η, and ζ directions
S	=	wing semispan
T	=	nondimensional static temperature
t	=	nondimensional time
U, V, W	=	contravariant velocity components
U_∞	=	freestream velocity
u, v, w	=	nondimensional Cartesian velocity components in the x, y, and z directions
u_1, u_2, u_3	=	u, v, w
$\langle \boldsymbol{V} \rangle$	=	time-averaged velocity vector
x, y, z	=	nondimensional Cartesian coordinates in streamwise, normal, and spanwise directions based on wing orientation (nondimensionalized by the mean aerodynamic chord, L_{mac})
x_{LE}	=	x coordinate of the local leading edge as measured from the apex
x_1, x_2, x_3	=	x, y, z
x^*	=	nondimensional chordwise distance from the local leading edge, $(x - x_{\text{LE}})/C^*$
x^*_{root}	=	nondimensional chordwise distance from the apex, x/C_{root}
α	=	angle of attack
α_f	=	implicit compact filter coefficient
Γ	=	implicit compact differencing coefficient
γ	=	specific heat ratio, 1.4 for air
δ_ξ, δ_η, δ_ζ	=	interpolation offsets in the ξ, η, and ζ directions
δ_{ij}	=	Kronecker delta function
$\delta^{(2)}_\xi$, $\delta^{(2)}_\eta$, $\delta^{(2)}_\zeta$	=	second-order finite difference operators in ξ, η, ζ
$\delta^{(6)}_\xi$, $\delta^{(6)}_\eta$, $\delta^{(6)}_\zeta$	=	sixth-order finite difference operators in ξ, η, ζ
Δ	=	particle image velocimetry gap distance
Δt	=	time-step size
η	=	nondimensional spanwise location, z/S
Λ	=	wing sweep angle
μ	=	nondimensional molecular viscosity coefficient
ξ, η, ζ	=	nondimensional body-fitted computational coordinates
ξ_x, ξ_y, ξ_z	=	metric coefficients of the coordinate transformation
η_x, η_y, η_z	=	metric coefficients of the coordinate transformation
ζ_x, ζ_y, ζ_z	=	metric coefficients of the coordinate transformation

Received 28 July 2010; revision received 27 December 2010; accepted for publication 4 January 2011.

*Research Aerospace Engineer, Computational Sciences Branch Air Vehicles Directorate. Associate Fellow AIAA.
†Technical Area Leader, Computational Sciences Branch Air Vehicles Directorate. Associate Fellow AIAA.
‡Research Aerospace Engineer, Computational Sciences Branch Air Vehicles Directorate. Associate Fellow AIAA.
§Research Assistant, Department of Mechanical Engineering and Mechanics.
¶Professor, Department of Mechanical Engineering and Mechanics. Member AIAA.

ρ = nondimensional fluid density
σ = interpolation order of accuracy
τ_{ij} = components of the viscous stress tensor
ϕ = general scalar quantity, temporal scheme parameter
$\langle\omega\rangle$ = time-averaged nondimensional vorticity
$\wedge$ = filtered value
$\overline{\ }$ = interpolated value

Subscripts

i = grid-point reference
p = interpolation point
∞ = dimensional reference value

Superscripts

n = time level
p = subiteration level

I. Introduction

UNMANNED combat air vehicles (UCAVs) possessing low-sweep delta-wing planforms continue to be of interest to the international aerospace community from both an experimental and computational perspective. Their three-dimensional configuration can give rise to complex flow patterns, whereby the occurrence of separation and stall can vary substantially along the span. Flow separation, transition from laminar to turbulent flow, and nonlinear vortex dynamics such as vortex interactions and breakdown are examples of the types of flow features that may be encountered when considering such geometries.

In recent years, the "1303" UCAV configuration, developed by the U.S. Air Force Research Laboratory in conjunction with The Boeing Company [1], has been examined using both experimental and computational techniques. Experimentally, wind-tunnel investigations at moderate Reynolds numbers have been performed by Bruce [2] and McParlin et al. [3] using a variety of leading-edge geometries, as well as by Ghee [4,5] and Ghee and Hall [6]. Ol [7] characterized the sectional flow structure at lower Reynolds numbers in terms of patterns of mean velocity and Reynolds stress using particle image velocimetry (PIV) in a water channel facility. Dye visualization of the processes of flow separation and vortex formation were addressed in a water facility by Nelson et al. [8]. Kosoglu [9] employed dye visualization to qualitatively describe the three-dimensionality, in conjunction with PIV, with emphasis on the flow structure in planes that were oriented parallel to the wing surface.

This geometry has also been studied computationally by a wide range of researchers as part of The Technical Cooperation Program under the auspices of the Aerospace Systems Group's Technical Panel 5 (AER TP-5) using both low-order structured [10–12] and unstructured codes [13] at the higher Reynolds numbers of Bruce [2]. The general conclusion drawn from these works was that the low-order computational fluid dynamics coupled with an appropriate turbulence model was effective at predicting the magnitudes of lift and drag forces at the lower angles of attack where the flow remains primarily attached, but was unable to maintain this performance at the higher angles where separation becomes more widespread. However, these works focused primarily on the prediction of force and moment coefficients and not as much on the flowfield structure associated with this geometry.

The foregoing investigations of the three-dimensional, 1303 UCAV are related to investigations in recent years on planar (flat) delta wings having low-to-moderate values of sweep angle. The flow structure on planar delta wings and UCAV planforms has been the subject of extensive experimental study. Reviews of these investigations are provided by Gursul [14,15] and Gursul et al. [16]. Experimental investigations on wings having various values of sweep angle in the low-to-moderate range, as well as on planar simplifications of UCAV configurations, have been addressed experimentally by Ol and Gharib [17], Yavuz et al. [18], and Yaniktepe and Rockwell [19,20]. Computations of the flow structure on delta wings of low sweep angle, with emphasis on lower values of Reynolds number, have been performed by Gordnier and Visbal [21] using a high-order, structured-grid, finite difference algorithm [22]. Gordnier and Visbal [23] and Gordnier et al. [24] have also addressed features of the flow structure of planar delta wings at moderate values of Reynolds number.

In the current work, the high-order algorithm of Gaitonde and Visbal [22] incorporating a general overset-grid capability that maintains the overall high-order accuracy of the solution [25] is used to simulate the flowfield over the 1303 UCAV geometry at various angle of attack and Reynolds numbers. The leading-edge geometry studied here is the "sharp" leading edge as defined by Bruce [2], which means that the leading-edge radius of curvature is less than 0.03 per cent of the mean aerodynamic chord. These simulations are compared with experimental data recently acquired from the free-surface water channel at Lehigh University. The high-order overset-grid solver has been applied to canonical problems with elementary geometries [25,26] as well as component-level studies involving more complex overset-grid topologies [27,28]. One of the goals of this study was to develop and validate computational tools to simulate a more realistic, but still relatively clean, complete aircraft using the high-order overset-grid algorithm. In addition, fundamental aerodynamic phenomena associated with the tailless, low-sweep 1303 configuration will be examined using the improved resolution of the high-order algorithm.

The organization of this paper is as follows. In Sec. II, the numerical procedures associated with the high-order overset grid used in this study will be presented. Details regarding the experimental setup and collection of data are then presented in Sec. III. The results are presented in Sec. IV, first focusing on the comparison of computational to experimental data, and then examining the mean flow structures. Finally, the conclusions are discussed in Sec. V.

II. Numerical Procedure

A. Governing Equations

The governing equations to be solved are given by the three-dimensional, unfiltered, unsteady, compressible Navier-Stokes equations. When normalized by the reference quantities ρ_∞, u_∞, μ_∞, L_{mac} and with the pressure normalized by $\rho_\infty u_\infty^2$, this set of equations may be written in strong conservation form for a general, time-invariant, curvilinear coordinate system (ξ, η, ζ) as [22]

$$\frac{\partial}{\partial t}\left(\frac{\boldsymbol{Q}}{\mathcal{J}}\right)+\frac{\partial \boldsymbol{F}}{\partial \xi}+\frac{\partial \boldsymbol{G}}{\partial \eta}+\frac{\partial \boldsymbol{H}}{\partial \zeta}=\frac{1}{Re}\left[\frac{\partial \hat{\mathbf{F}}_v}{\partial \xi}+\frac{\partial \hat{\mathbf{G}}_v}{\partial \eta}+\frac{\partial \hat{\mathbf{H}}_v}{\partial \zeta}\right] \tag{1}$$

The solution vector in the above equation is given by $\boldsymbol{Q}=\{\rho, \rho u, \rho v, \rho w, \rho E_t\}^T$, while the inviscid and viscous flux vectors are given by

$$\boldsymbol{F}=\frac{1}{\mathcal{J}}\begin{bmatrix}\rho U\\ \rho u U+\xi_x p\\ \rho v U+\xi_y p\\ \rho w U+\xi_z p\\ \rho E_t U+pU\end{bmatrix} \quad \boldsymbol{G}=\frac{1}{\mathcal{J}}\begin{bmatrix}\rho V\\ \rho u V+\eta_x p\\ \rho v V+\eta_y p\\ \rho w V+\eta_z p\\ \rho E_t V+pV\end{bmatrix}$$

$$\boldsymbol{H}=\frac{1}{\mathcal{J}}\begin{bmatrix}\rho W\\ \rho u W+\zeta_x p\\ \rho v W+\zeta_y p\\ \rho w W+\zeta_z p\\ \rho E_t W+pW\end{bmatrix} \tag{2}$$

and

$$\boldsymbol{F}_v = \frac{1}{\mathcal{J}}\begin{bmatrix} 0 \\ \xi_{x_i}\tau_{i1} \\ \xi_{x_i}\tau_{i2} \\ \xi_{x_i}\tau_{i3} \\ \xi_{x_i}q_i \end{bmatrix} \qquad \boldsymbol{G}_v = \frac{1}{\mathcal{J}}\begin{bmatrix} 0 \\ \eta_{x_i}\tau_{i1} \\ \eta_{x_i}\tau_{i2} \\ \eta_{x_i}\tau_{i3} \\ \eta_{x_i}q_i \end{bmatrix} \qquad \boldsymbol{H}_v = \frac{1}{\mathcal{J}}\begin{bmatrix} 0 \\ \zeta_{x_i}\tau_{i1} \\ \zeta_{x_i}\tau_{i2} \\ \zeta_{x_i}\tau_{i3} \\ \zeta_{x_i}q_i \end{bmatrix} \tag{3}$$

With x_i and ξ_i $(i = 1, 2, 3)$ used to represent (x, y, z) and (ξ, η, ζ), respectively, the stress tensor and heat flux vector may be written as

$$\tau_{ij} = \mu\left(\frac{\partial \xi_k}{\partial x_j}\frac{\partial u_i}{\partial \xi_k} + \frac{\partial \xi_k}{\partial x_i}\frac{\partial u_j}{\partial \xi_k} - \frac{2}{3}\delta_{ij}\frac{\partial \xi_l}{\partial x_k}\frac{\partial u_k}{\partial \xi_l}\right) \tag{4}$$

and

$$q_i = -\frac{1}{(\gamma-1)M_\infty^2}\frac{\mu}{Pr}\frac{\partial \xi_l}{\partial x_i}\frac{\partial T}{\partial \xi_l} \tag{5}$$

The contravariant velocity components and total energy are written as

$$\begin{aligned} U &= \xi_x u + \xi_y v + \xi_z w \\ V &= \eta_x u + \eta_y v + \eta_z w \\ W &= \zeta_x u + \zeta_y v + \zeta_z w \end{aligned} \tag{6}$$

and

$$E_t = \frac{T}{(\gamma-1)M_\infty^2} + \frac{1}{2}(u^2 + v^2 + w^2) \tag{7}$$

respectively. The equation of state for a perfect gas is employed, as is Sutherland's law for the molecular viscosity μ. A constant Prandtl number of $Pr = 0.72$ is also assumed.

In standard compressible LES, the governing equations are filtered using a grid-filtering function and Favre-averaged variables are introduced. Additional subgrid-scale stress and heat flux models are then introduced to capture the turbulent behavior of the scales not resolved by the computational grid. In this work, however, an alternative approach is taken where the energy present at the poorly resolved smallest scales of the flow is dissipated through the use of a high-order, low-pass, implicit spatial filter [29]. Although the filter is applied explicitly to the evolving solution, the approach is considered to be an implicit LES method. This is due to the fact that the application of a spatial filter is a fundamental component of the algorithm which removes high-frequency, spurious numerical oscillations to maintain stability. Details on the spatial filter are given later in this section.

B. Spatial Differencing Formulas

The set of equations in Eq. (1) is discretized using a finite difference approach based on the Padé-type compact finite difference formulations of Lele [30] as implemented by Gaitonde and Visbal [22,31] and Visbal and Gaitonde [32]. On the interior of the computational domain, the spatial derivative ϕ' of any scalar quantity ϕ may be found at the node points in computational space by solving the tridiagonal system arising from the formula

$$\Gamma\phi'_{i-1} + \phi'_i + \Gamma\phi_{i+1} = b\frac{\phi_{i+2} - \phi_{i-2}}{4} + a\frac{\phi_{i+1} - \phi_{i-1}}{2} \tag{8}$$

The coefficients Γ, a, and b in Eq. (8) determine the spatial order of accuracy of the first-derivative computation, as well as whether they are found in an explicit or implicit manner. Here, the implicit interior scheme used to calculate first-order derivatives is a compact, five-point, sixth-order scheme, where $\Gamma = \frac{1}{3}$, $a = \frac{14}{9}$, and $b = \frac{1}{9}$. For points located on or one point away from computational boundaries, the five-point centered formula given by Eq. (8) cannot be applied. At these points, high-order one-sided formulations are used to maintain at least fourth-order accuracy at the boundary points. An explicit second-order scheme is also used in this study, with $\Gamma = 0$, $a = 1$, and $b = 0$. More detail regarding these boundary formulations may found in Gaitonde and Visbal [22].

The derivatives of the inviscid fluxes are found by first calculating the fluxes at the nodes, and then differentiating each component via application of Eq. (8). For the viscous terms, the primitive variables u, v, w, and T are differentiated using Eq. (8) to form the components of the stress tensor and heat flux vector at each node. These values are then used to form the viscous flux vectors, and each component is then differentiated using the same differencing method to find the derivatives of the viscous flux vectors at the nodes.

C. Filtering Formulas

Because the schemes generated by Eq. (8) are centered, they are nondissipative in nature. Thus, numerical instabilities arising from poor grid quality, unresolved scales, or boundary conditions will be left to grow unchecked and can potentially corrupt the solution. For this reason, a low-pass symmetric filter of up to 10th-order accuracy of the form

$$\alpha_f\hat{\phi}_{i-1} + \hat{\phi}_i + \alpha_f\hat{\phi}_{i+1} = \sum_{n=0}^{N}\frac{f_n}{2}(\phi_{i+n} + \phi_{i-n}) \tag{9}$$

is applied on the interior of the domain in each of the three coordinate directions after each subiteration to remove spurious high-frequency waves and maintain solution integrity. The coefficient α_f is a free parameter in the range of $-0.5 < \alpha_f \leq 0.5$ that may be used to control the spectral response of the filter [22,32] as well as whether the filter will be implicit ($\alpha_f \neq 0$, resulting in a tridiagonal system of equations) or explicit ($\alpha_f = 0$). As the value of α_f decreases from its maximum permissible value of 0.5 (where no filtering takes place), more energy content is removed over a wider range of wave number. The value of the coefficients $\{f_0, f_1, \ldots, f_N\}$ for centered filters of various orders of accuracy are given in Gaitonde and Visbal [22] as a function of α_f. Because of the symmetric form of Eq. (9) and the fact that they are being employed on the uniform mesh of computational space, the interior filters are nondispersive, do not amplify waves at any wave number, and result in the complete annihilation of the odd-even mode.

A 10th-order centered filter represented by Eq. (9) requires an 11-point stencil, and thus cannot be applied at nodes within five points of a computational boundary. At these points, a centered stencil may be retained at the cost of reducing the order of accuracy of the filter as the boundary is approached, or higher order one-sided filter formulations may be employed. The former approach was found to provide satisfactory results [32] for a variety of single-grid problems through the judicious use of grid clustering near boundaries. However, this approach is unacceptable when using a domain-decomposition approach to provide parallel-processing capability, due to the appearance of computational boundaries in areas of the domain that would not otherwise be refined. The technique of employing one-sided, high-order filters near boundaries was proven effective for maintaining solution integrity in various overlapping-grid problems [31,33,34], and will be used here. The formulations for the various orders of accuracy of the one-sided, Padé-type filters are given in Gaitonde and Visbal [31] as a function of α_f.

D. Temporal Integration

The high-order overset-grid solver uses either an implicit up-to-third-order approximately factored Beam–Warming method [35] or an explicit fourth-order Runge–Kutta method implemented in low-storage form [36] to advance the solution in time. As the problem considered in this work involves simulation of viscous, wall-bounded flows using significant grid clustering, only the implicit solver was employed. In delta form, this method may be expressed as

$$\left[\boldsymbol{I}+\phi^i\Delta t\delta_\xi^{(2)}\left(\frac{\partial \boldsymbol{F}^p}{\partial \boldsymbol{Q}}-\frac{1}{Re}\frac{\partial \boldsymbol{F}_v^p}{\partial \boldsymbol{Q}}\right)\right]\left[\boldsymbol{I}+\phi^i\Delta t\delta_\eta^{(2)}\left(\frac{\partial \boldsymbol{G}^p}{\partial \boldsymbol{Q}}-\frac{1}{Re}\frac{\partial \boldsymbol{G}_v^p}{\partial \boldsymbol{Q}}\right)\right]$$
$$\times\left[\boldsymbol{I}+\phi^i\Delta t\delta_\zeta^{(2)}\left(\frac{\partial \boldsymbol{H}^p}{\partial \boldsymbol{Q}}-\frac{1}{Re}\frac{\partial \boldsymbol{H}_v^p}{\partial \boldsymbol{Q}}\right)\right]\Delta\boldsymbol{Q}$$
$$=-\phi^i\Delta t\left[\frac{(1+\phi)\boldsymbol{Q}^p-(1+2\phi)\boldsymbol{Q}^n+\phi\boldsymbol{Q}^{n-1}}{\Delta t}\right.$$
$$+\delta_\xi^{(6)}\left(\boldsymbol{F}^p-\frac{1}{Re}\boldsymbol{F}_v^p\right)+\delta_\eta^{(6)}\left(\boldsymbol{G}^p-\frac{1}{Re}\boldsymbol{G}^p\right)$$
$$\left.+\delta_\zeta^{(6)}\left(\boldsymbol{H}^p-\frac{1}{Re}\boldsymbol{H}_v^p\right)\right] \tag{10}$$

where $\phi^i = 1/(1+\phi)$, with $\phi = 0$ and 1/2 for the first-order Euler implicit and second-order three-point backward schemes, respectively. Newton-like subiterations [37] are employed to maintain temporal accuracy and reduce error arising from linearization, factorization, diagonalization, and explicit implementation of boundary conditions at both physical and computational domain boundaries. The subiteration level in Eq. (10) is referenced by the superscript p, with $\Delta\boldsymbol{Q} = \boldsymbol{Q}^{p+1} - \boldsymbol{Q}^p$, $\boldsymbol{Q}^p = \boldsymbol{Q}^n$ at $p = 1$, and $\boldsymbol{Q}^p = \boldsymbol{Q}^{n+1}$ as $p \to \infty$. The diagonalized form of the approximately factored scheme [38] is employed to improve efficiency. The implicit portion of the algorithm uses second-order centered finite differencing for the spatial derivatives, indicated by the $\delta^{(2)}$ operator notation. The spatial derivatives on the right-hand side of Eq. (10) are evaluated using centered sixth-order finite differences calculated in each coordinate direction with Eq. (8), indicated by the $\delta^{(6)}$ operator. Nonlinear second- and fourth-order artificial dissipation terms are added to the implicit operator only in Eq. (10) for stability purposes. However, the use of subiterations severely reduces the impact of the implicit damping on the solution, as well as the degradation due to the use of low-order spatial derivatives in the implicit operators.

E. Overset Methodology

An overset-grid approach is used to provide flexibility for modeling complex geometries. It also serves as a domain-decomposition mechanism for application of the high-order approach on massively parallel computing platforms [34]. The first step in this method is to generate overset structured grids based on the physical geometry of the problem. Typically, these consist of individual body-fitted grids around each geometric feature of interest and a background grid in which the body-fitted grids are embedded. Additional grids can be included to provide better resolution in key areas or for other specific purposes. In general, the points in the overlapping regions between grid components are noncoincident.

Once the grids are established based on the physical requirements of the problem, the connectivity between grids is established using spatially-second-order-accurate connectivity software [39]. This second-order connectivity data then serves as input for a subsequent preprocessing code [40], which expands the computational stencils and computes the high-order interpolation offsets and coefficients. The high-order interpolation approach used here is a general three-dimensional explicit interpolation formula given by

$$\bar{\phi}_p = \sum_{i,j,k=0}^{\sigma-1} R_k^\zeta(\delta_\zeta)\cdot R_j^\eta(\delta_\eta)\cdot R_i^\xi(\delta_\xi)\cdot\phi_{I_p+i,J_p+j,K_p+k} \tag{11}$$

that yields the interpolated primitive flowfield variable $\bar{\phi}_p$ at an interpolation point p using the known functional values ϕ at a set of donating stencil points based on the donor point (I_p, J_p, K_p). The parameter σ is the formal order of accuracy of the interpolation method, and also equals the number of stencil points in each coordinate direction. The interpolation coefficients are given by the analytical expression

$$R_n^x = \frac{(-1)^{\sigma+n-1}}{[\sigma-(n-1)!]n!}\prod_{\substack{i=0\\ i\neq n}}^{\sigma-1}(\delta_x - i) \tag{12}$$

The offsets δ in each coordinate direction are computed using an iterative high-order inverse parametric mapping [41] using the expanded stencils and the original low-order offsets as an initial guess.

The preprocessing code also handles partitioning the grids into overlapping blocks for parallel processing, with each block assigned to a single processor. Communication between blocks residing on the same grid is handled though finite-sized overlaps consisting of coincident grid points. Thus, no interpolation is required per se at block boundaries, as data is exchanged exactly between coincident points as needed. Two-point fringes are employed at all interpolation boundaries (grid, block, or hole); based on previous studies [31], this is sufficient to recover the interior high-order differencing and filtering of the original single-grid algorithm. Even though no interpolation is required between the coincident points residing on adjacent blocks, the communication between such points is handled using the same overset-grid infrastructure in the flow solver. Thus, the establishment of the connectivity of the overall block-level system is fundamentally a two-part process; direct-injection donor-receiver pairs arising from the decomposition of the grids into blocks are identified, and the grid-level connectivity for the noncoincident

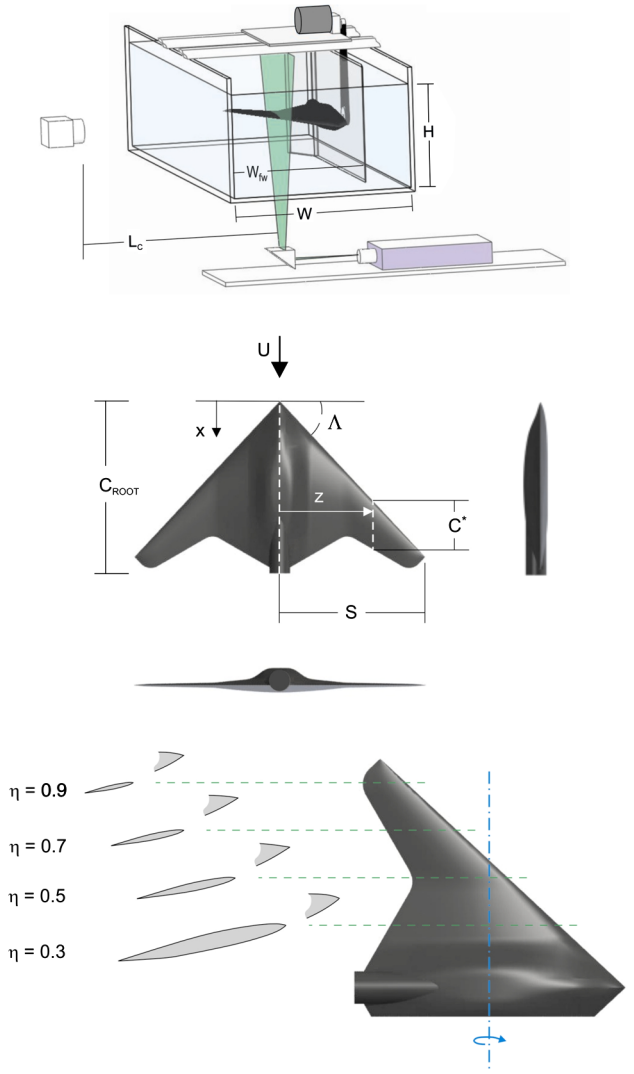

Fig. 1 Overview of experimental system showing arrangement for particle image velocimetry system in relation to half-wing mounted in water channel, and definitions of parameters and zoomed-in views of half-wing in relation to full wing (from Yilmaz and Rockwell [44]).

interpolation points established by the low-order connectivity software is transformed into the block-level system. The data created by both of these steps is then combined to produce the overall block-level connectivity.

The preprocessing code also performs some additional functions as well, including decomposition of the grid-level boundary conditions to block-level, and storage of hole boundary points in each of the coordinate directions. Hole-cutting [42] is incorporated into the algorithm by decoupling the points located inside a hole from the field points outside of the hold in the implicit spatial algorithm. Then the centered differencing and filtering formulations are replaced with their appropriate one-sided counterparts at the hole boundaries [43]. Communication in the flow solver is performed using the Message-Passing Interface communications library with the block-level connectivity data generated as discussed in the previous paragraph.

III. Experimental System and Techniques

A free-surface water channel was employed for the experiments conducted as part of this effort. The test section has a length of 5435 mm, a width of 613 mm, and a height of 594 mm. To attain relatively low values of turbulence intensity, of the order of 0.3%, a system of honeycomb and five screens were positioned at a location upstream of the main contraction of the water channel facility. In the present experiments, the value of the freestream velocity varied over the range $80 \leq U_\infty \leq 246$ mm/s.

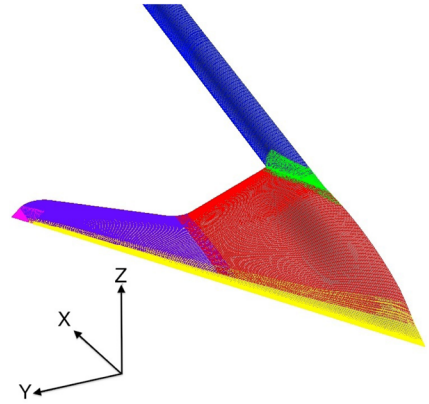

a) Surface grids

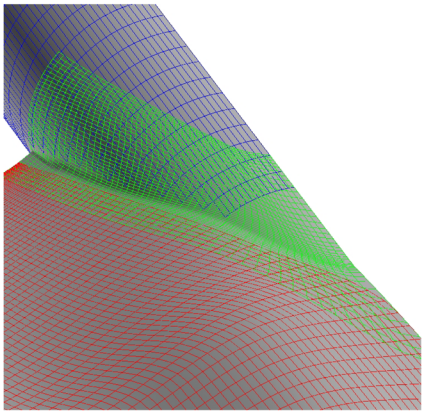

b) Close-up of collar surface grid

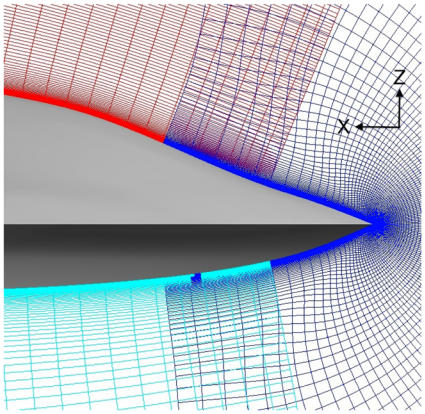

c) Close-up of volume grids in nose region

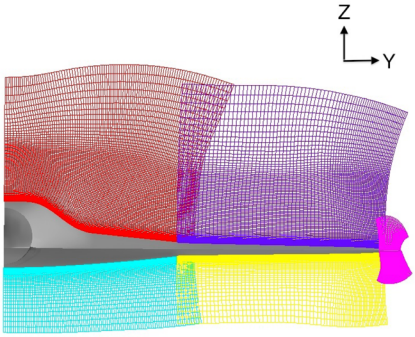

d) Volume grids above and below wing

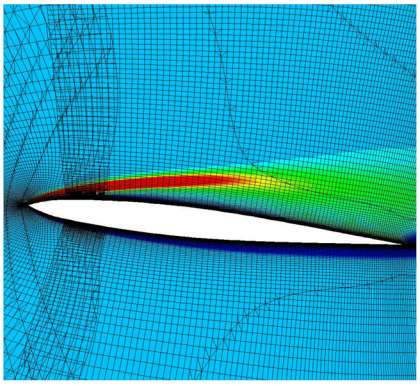

e) Cell spacing at $\eta = 0.8$ plane superimposed over mean spanwise-normal velocity at $\alpha = 6^o$, $Re_{mac} = 29879$

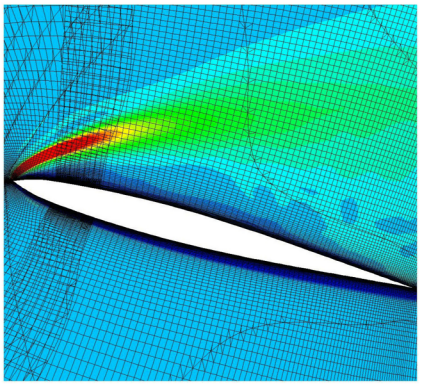

f) Cell spacing at $\eta = 0.8$ plane superimposed over mean spanwise-normal velocity at $\alpha = 15^o$, $Re_{mac} = 29879$

Fig. 2 Overset-grid system for 1303-UCAV simulation.

Figure 1 shows various representations of the three-dimensional 1303 UCAV model, and its mounting within the water channel. A partial wing was fixed to a rotatable disk mounted in the wall of a vertical support plate, thereby allowing adjustment to arbitrary angle of attack α. The wing had a sweep angle of $\Lambda = 47°$ and a semispan of $S = 300$ mm. Furthermore, the root chord was $C_{\text{root}} = 355.6$ mm. The arrangement shown in Fig. 1 minimizes the influence of the approach boundary layer along the vertical support plate. This was accomplished by employing the indicated wing configuration, which allows the geometrical plane of symmetry of the wing, i.e., the plane passing through the centerbody of the wing, to be displaced from the surface of the plate by a distance of $\Delta = 38.1$ mm. Since the wing was mounted at a location immediately downstream of the leading edge of the vertical support plate, the displacement thickness of the approach boundary layer was measured to be an order of magnitude smaller than the gap Δ. The plane passing through the centerbody of the 1303 UCAV model indicated in Fig. 1 represents, in essence, a plane of zero normal velocity, verified by dye visualization and PIV measurements, in comparison with a full wing configuration, as described in detail by Yilmaz and Rockwell [44]. For this wing arrangement within the aforementioned test section of the water channel, as shown in Fig. 1, the blockage ratio of the wing varied from 0.026 to 0.054 at angles of attack $\alpha = 0$ to 12°.

For the present experiments, data were collected at various angles of attack, while the Reynolds numbers based on mean aerodynamic chord were $Re_{\text{mac}} = 17,927$, 29,879, and 59,758, corresponding to values based on root chord of $Re_{C_{\text{root}}} = 3 \times 10^4$, 5×10^4, and 1×10^5. The leading edge for the current model is the sharp case in the lexicon of Bruce 2 (a leading-edge radius of curvature of less than 0.03 per cent of the mean aerodynamic chord), which fixes the separation location at the leading edge of the wing.

To determine the quantitative patterns of the flow structure, a technique of particle image velocimetry was employed. Figure 1 designates the location and orientation of the laser sheet. Images were acquired at various values of dimensionless spanwise locations $\eta = z/S$ by mounting the laser on a traverse system. Optimization of the quality of the patterns of particle images for PIV requires proper filtering of water, which was performed with a 1 μm filter system. After the filtered water was naturally degassed, it was seeded with 12-μm-diam metallic-coated plastic spheres. The seeding density ensured that a minimum of approximately 15 particle images were present within the interrogation window of 32×32 pixels during the PIV interrogation process. The suspended spheres were illuminated by a dual-pulsed YAG laser system, which had a pulse rate of 29 Hz, thereby yielding 14.5 pairs of images of the particle patterns per second. The YAG laser had a maximum power output of 90 mJ.

The patterns of particle images were evaluated using a frame-to-frame cross-correlation technique, in order to obtain patterns of instantaneous velocity vectors. The interrogation window had a size of 32×32 pixels, and in order to satisfy the Nyquist criterion, a 50% overlap was employed. Acquisition of images at different locations $\eta = z/S$ along the span of the wing involved adjustment of the distance between the physical plane of the laser sheet and the sensor array. For the present investigation, this distance had a minimum value of 456 mm and a maximum value of 670 mm. Values of $\eta = 0.7$, 0.8, and 0.9 correspond to values of magnification of 13.41, 15.71, and 19.77 pixels/mm and, furthermore, grid sizes (distances between locations of velocity vectors) of 2.38, 2.04, and 1.62 mm. The foregoing parameters correspond to the following fields of view in the physical plane of the laser sheet: 108×67 mm, 94×61 mm, and 75×43 mm at $\eta = 0.7$, 0.8, and 0.9, respectively. For all

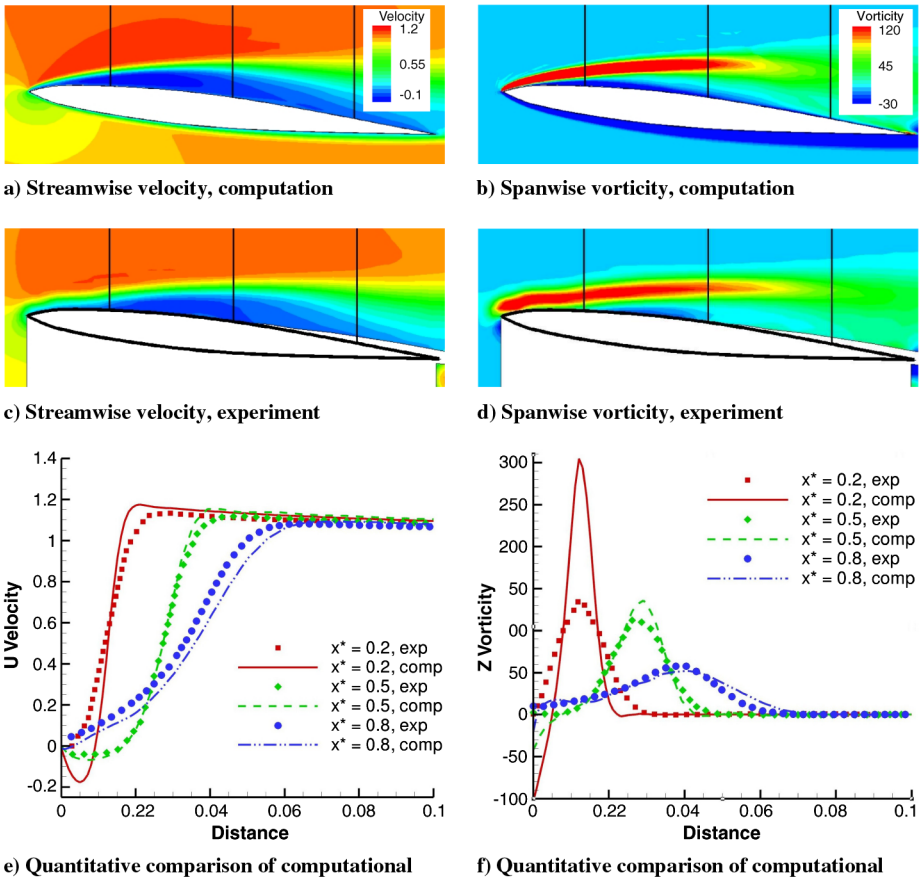

a) Streamwise velocity, computation

b) Spanwise vorticity, computation

c) Streamwise velocity, experiment

d) Spanwise vorticity, experiment

e) Quantitative comparison of computational and experimental data, streamwise velocity

f) Quantitative comparison of computational and experimental data, spanwise vorticity

Fig. 3 Comparison of mean streamwise velocity (left) and mean spanwise-normal vorticity (right) between computation and experiment at the spanwise station $\eta = 0.8$ for $\alpha = 6°$ and $Re_{\text{mac}} = 29,879$. Black vertical lines represent streamwise stations for quantitative comparisons.

experiments, the same imaging camera was employed; it had a pixel array of 1600×1200 pixels. The uncertainty of the velocity measurements is estimated to be 1.5%.

To determine the time-averaged patterns of velocity vectors $\langle \boldsymbol{V} \rangle$, an average was taken of 200 images. These patterns of $\langle \boldsymbol{V} \rangle$ were employed to determine the patterns of time-averaged vorticity $\langle \omega \rangle$ and contours of streamwise velocity $\langle u \rangle$. These values were calculated from the time-averaged representations of the velocity vectors.

IV. Results

A. Computational Details

Flow over the 1303 UCAV configuration was computed at various angles of attack and Reynolds numbers. Cases run using the high-order algorithm specifically refer to the compact sixth-order spatial differencing algorithm with a 10th-order interior filter ($\alpha_f = 0.4$) and fourth-order interpolation $\sigma = 4$ at all interpolation boundaries. For all cases shown here, the second-order implicit Beam–Warming algorithm in diagonal form was employed with $\Delta t = 0.0002$ and three Newton subiterations per time step. All cases were started impulsively from uniform freestream flow at the specified angle of attack. The flow was allowed to develop for 20 characteristic times to eliminate transients associated with the impulsive startup before averaging and turbulent statistic collection. Each case was run for another 20 characteristic times in order to gather statistics and calculate averages (the exception being the 12° angle-of-attack case at $Re_{\text{mac}} = 59,758$, which was only averaged over 14 characteristic times, due to a data-corruption issue).

A single overset-grid topology consisting of 15 grids and approximately 10.8 million grid points was developed for the symmetric half-span UCAV configuration. This grid system consists of two main wing grids on each of the top and bottom of the geometry, a set of three grids that encapsulate the wingtip, a grid that wraps around the leading edge (which could be replaced without modifying the rest of the topology and would allow quick modification to the leading-edge geometry for potential future studies), two collar grids (top and bottom) at the junction of the sting and the aft body, a wake grid downstream of the trailing edge of the wing, two cylindrical sting grids, and both near- and far-field background grids. Views of various surface grids and offbody volumetric grids are shown in Fig. 2. Surface patches were generated manually using commercial grid generation tools. Body-fitted grids were subsequently generated using a hyperbolic marching algorithm using a wall-normal spacing of 0.0001 at all solid-wall boundaries. For the inboard and outboard grids on leeward side of the wing, the stretching ratio used in marching away from the solid surface was set to a value of 1.1 for the first 42 points and then was reduced to a value of 1.0 in order to provide additional resolution in the anticipated region of the leading-edge vortex system above the wing. The nominal grid spacing in the normal direction in this region was given by approximately 0.005. Once the hyperbolic marching reached approximately 0.25 nondimensional heights above the wing surface using this relatively uniform spacing, the stretching ratio was once again set to 1.1. On the inboard and outboard wing grids on the windward side of the UCAV, the grids were uniformly stretched using a stretching ratio of 1.1. A cutaway view of the inboard and outboard wing grids on both sides of the UCAV, including the top and bottom wingtip grids, is seen in

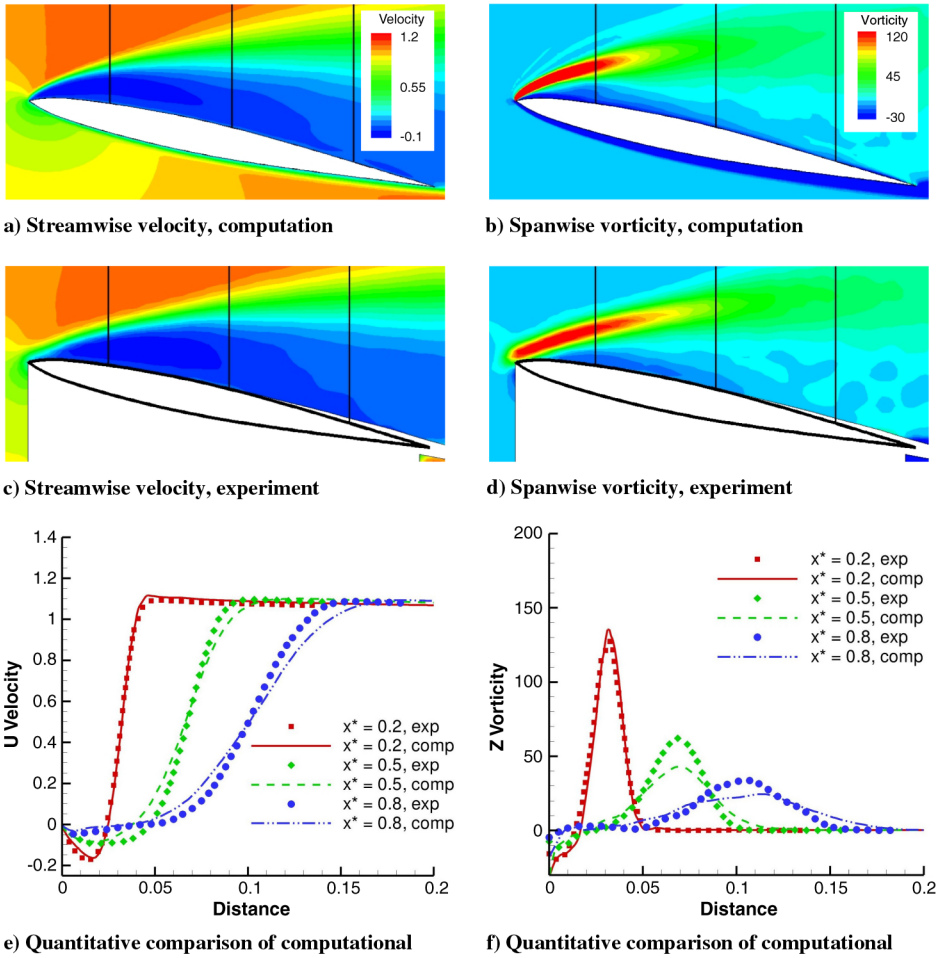

a) Streamwise velocity, computation

b) Spanwise vorticity, computation

c) Streamwise velocity, experiment

d) Spanwise vorticity, experiment

e) Quantitative comparison of computational and experimental data, streamwise velocity

f) Quantitative comparison of computational and experimental data, spanwise vorticity

Fig. 4 Comparison of mean streamwise velocity (left) and mean spanwise-normal vorticity (right) between computation and experiment at the spanwise station $\eta = 0.8$ for $\alpha = 12°$ and $Re_{\text{mac}} = 29,879$. Black vertical lines represent streamwise stations for quantitative comparisons.

Fig. 2d and shows the extents of these regions. The current grid system represents a significant increase in complexity from geometries previously examined with this high-order overset-grid approach.

The boundary conditions for this problem were specified in the following manner. At solid surfaces, no-slip conditions were applied (i.e., $u = v = w = 0$) and the wall was assumed to be isothermal with a normal pressure gradient condition $\partial p/\partial n = 0$ specified. Symmetry conditions ($w = 0$, $[\partial(u, v, p, \rho)/\partial z] = 0$) were employed on the symmetric $\eta = 0$. The Neumann-type boundary conditions at the wall and symmetry plane were evaluated using second-order derivatives for the low-order cases and fourth-order derivatives for the high-order cases. On the inflow and lower boundaries, uniform flow was specified, whereas at the outflow, upper, and side boundaries, all variables were extrapolated from the interior using a first-order extrapolation. The treatment of the far-field boundaries was based on the approach proposed and evaluated previously [45] for some acoustic benchmark problems. This method exploits the properties of the high-order, low-pass filter in conjunction with a rapidly stretched mesh. As grid spacing increases away from the region of interest, energy not supported by the stretched mesh is reflected in the form of high-frequency modes which are annihilated by the discriminating spatial filter operator. An effective buffer zone is therefore created using a few grid points in each coordinate direction to rapidly stretch to the far-field boundary. No further need for the explicit incorporation of complicated boundary conditions or modifications to the governing equations is then required.

B. Comparison with Averaged Experimental Data

Computations were performed at three Reynolds numbers ($Re_{\text{mac}} = 17,927$, 29,879 and 59,758) and at three angles of attack ($\alpha = 6$, 12, and 15°). These values correspond to experimental data sets collected in the water tunnel discussed in Sec. III. Initial runs were performed on all nine cases in the test matrix; however, only five cases were run out to statistical and average convergence and will be presented here. These five cases allowed for a range of Reynolds numbers to be considered at a fixed angle of attack, and for a range of angles of attack to be considered at a fixed Reynolds number. The cases presented here are $Re_{\text{mac}} = 17,927$, 29,879, and 59,758 at $\alpha = 12°$ and $Re_{\text{mac}} = 29,879$ at $\alpha = 6$, 12, and 15°.

1. *Angle-of-Attack Variation at Fixed Re_{mac}*

First, comparisons are made between the current computations and the experiments for the three angles of attack under consideration at $Re_{\text{mac}} = 29,879$. Emphasis is on comparisons between computational and experimental results at the discrete spanwise plane on the outer region of the wing at 80% of the half-span ($\eta = 0.8$). Additional comparisons at stations $\eta = 0.7$ and 0.9 may be found in Sherer et al. [46].

Qualitative and quantitative comparisons for the mean streamwise velocity and the spanwise-normal component of vorticity (Z vorticity) at the $\eta = 0.8$ spanwise plane is presented in Figs. 3–5 for the various angles of attack at $Re_{\text{mac}} = 29,879$. The dark black airfoil shape within the masked-out region of the experimental data

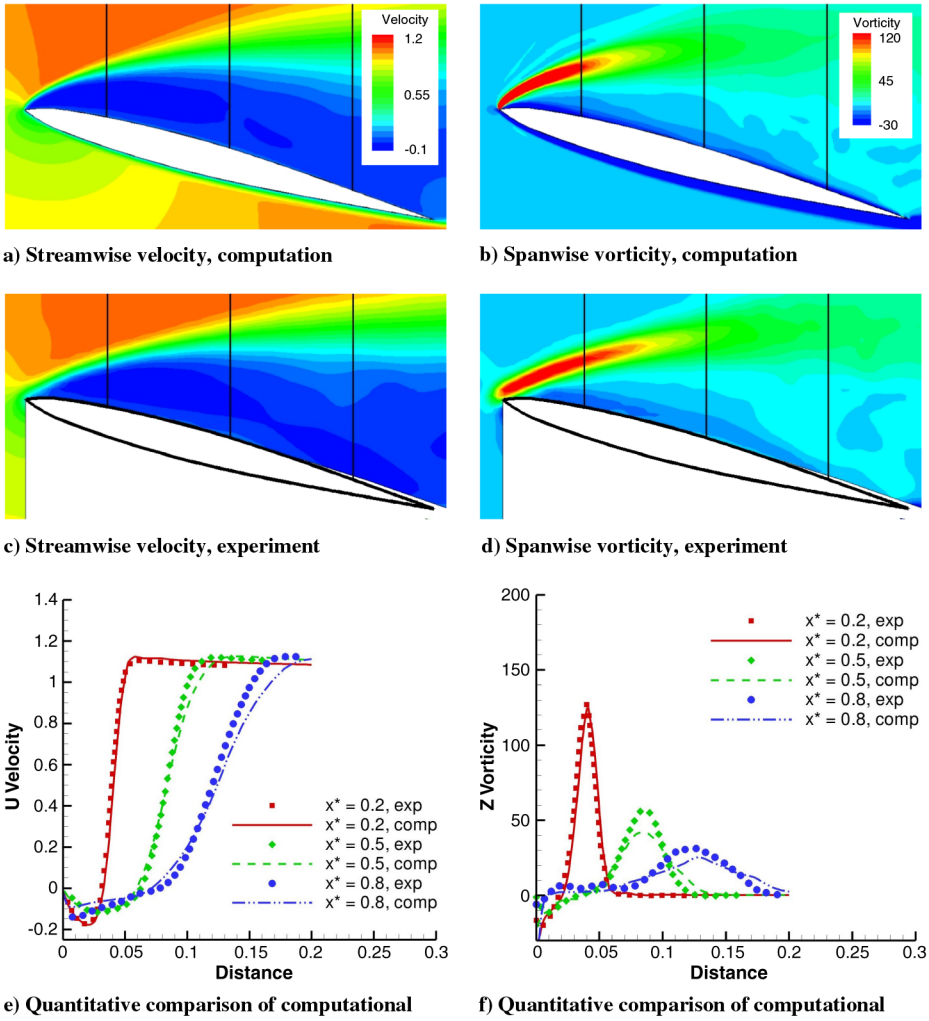

a) Streamwise velocity, computation

b) Spanwise vorticity, computation

c) Streamwise velocity, experiment

d) Spanwise vorticity, experiment

e) Quantitative comparison of computational and experimental data, streamwise velocity

f) Quantitative comparison of computational and experimental data, spanwise vorticity

Fig. 5 Comparison of mean streamwise velocity (left) and mean spanwise-normal vorticity (right) between computation and experiment at the spanwise station $\eta = 0.8$ for $\alpha = 15°$ and $Re_{\text{mac}} = 29,879$. Black vertical lines represent streamwise stations for quantitative comparisons.

represents the approximate relative position of the airfoil cross section. The quantitative comparisons between computational and experimental results are performed at the streamwise locations along the upper surface of the wing indicated by the three black vertical lines at values of $x^* = 0.2$, 0.5, and 0.8, where x^* is the chordwise distance from the leading-edge nondimensionalized by the local chord ($x^* = (x - x_{LE})/C^*$). The comparison between experiment and computation for both mean velocity and mean vorticity at all spanwise stations shown here are quite good, particularly at $\alpha = 12$ and 15°. At $\alpha = 6°$, the computational results tend to overpredict the vorticity present in the shear layer compared with the experiment when the shear layer is still close to the body (Fig. 3f at $x^* = 0.2$ and 0.5). This may be due to the onset of a small-amplitude flapping instability in the experimental environment which results in thickening of the time-averaged shear layer and a decrease in the measured value of peak mean vorticity. Evidence of this is observed in the shape of the shear layer, as represented by the region of high mean spanwise vorticity in Fig. 3d. Near the leading edge of the wing, the experimental shear layer exhibits a more irregular shape at $\alpha = 6°$, as compared with the smoother representations of the shear layer at higher angles of attack, suggesting the onset of an instability in the experiment at this angle of attack. This hypothesized instability may involve a combination of the inherent hydrodynamic instability of the separated shear layer and undulation of the shear layer, due to its tendency to reattach to the surface of the wing. At higher values of angle of attack, the separated shear layer does not tend to reattach, and therefore such self-excited undulations do not occur. This proposed concept deserves further investigation.

At $\alpha = 12$ and 15°, the general trend is that the velocity and vorticity profiles match very well at $x^* = 0.2$, where the shear layer is the strongest and closest to the surface of the three stations examined. However, at $x^* = 0.5$ and 0.8 the computation generally results in a more diffuse velocity profile, compared with the experiment. This is attributed to the fact that the grid resolution in the constant-normal-spacing region above the wing is likely not sufficient to fully resolve the shear layer as it moves away from the body at the higher angles of attack. As can be seen in Fig. 2e, which shows the grid cells at the $\eta = 0.8$ plane, the shear layer for the $\alpha = 6°$ case is almost entirely contained in the region of clustered grid spacing in the normal direction near the body. From Fig. 3f, the shear-layer peak magnitude is predicted quite well at $x^* = 0.5$ and 0.8, with a slight overprediction of the peak vorticity magnitude at $x^* = 0.5$, due to the previously hypothesized flapping instability in the experimental results. In the $\alpha = 12$ and 15° cases, the shear layer at $x^* = 0.5$ and 0.8 is entirely contained in the region of constant normal spacing (see Fig. 2f for the $\alpha = 15°$ case), thus leading to the conclusion that the grid spacing in this region is slightly underresolving the shear layer here.

2. Re_{mac} Variation at Fixed Angle of Attack

To investigate the effect of Reynolds number variation, the mean streamwise velocity and spanwise-normal vorticity component are plotted both qualitatively and quantitatively in Figs. 6 and 7 for the Reynolds numbers of $Re_{mac} = 17,927$ and 59,758 at a fixed angle of attack of $\alpha = 12°$. Plots for the case $\alpha = 12°$ at $Re_{mac} = 29,879$ may be found in Fig. 4. Again, the computational data is seen to agree qualitatively with the experimental data across the range of Reynolds numbers at $\eta = 0.8$. The decrease in peak vorticity magnitude, and the broadening and reduced extent of the shear layer with increasing

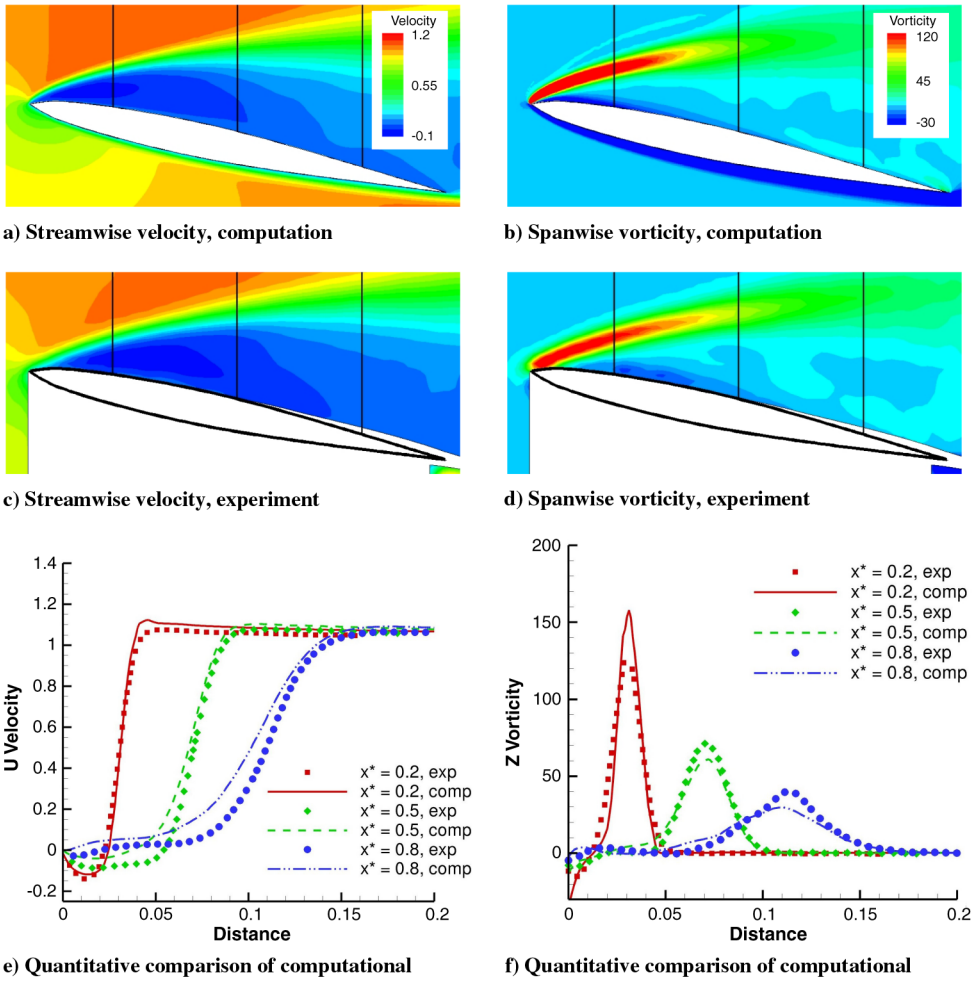

a) Streamwise velocity, computation

b) Spanwise vorticity, computation

c) Streamwise velocity, experiment

d) Spanwise vorticity, experiment

e) Quantitative comparison of computational and experimental data, streamwise velocity

f) Quantitative comparison of computational and experimental data, spanwise vorticity

Fig. 6 Comparison of mean streamwise velocity (left) and mean spanwise-normal vorticity (right) between computation and experiment at the spanwise station $\eta = 0.8$ for $\alpha = 12°$ and $Re_{mac} = 17,927$. Black vertical lines represent streamwise stations for quantitative comparisons.

Reynolds number are particularly visible. The general trend of the computations showing slightly higher vorticity levels toward the leading edge and slightly lower vorticity levels farther downstream when compared with the experimental data is maintained for these cases as well.

C. Instantaneous Results

In Fig. 8 the instantaneous isosurfaces of vorticity are shown shaded by the streamwise velocity for the five cases considered here. The sequence of Figs. 8a, 8c, and 8d offers a visual representation of the impact of increasing angles of attack, while Figs. 8b, 8c, and 8e show the effect of increasing Reynolds number. As the angle of attack increases, one can see the increase in the separated flow region at the wingtips, the upstream movement of the centerbody separation region, and the formation of the inboard vortical system. There is no inboard vortex visible at $\alpha = 6°$, while at $\alpha = 15°$ coherent streamwise structures are clearly visible inboard at the wing/centerbody junction. The $\alpha = 12°$ case represents a transitional situation between the low and high angles of attack where some streamwise structure is becoming visible inboard but has yet to form a coherent streamwise vortex. More detail on the formation of the inboard vortical system will be presented in a subsequent section.

The appearance of smaller flow scales and the onset of larger regions of turbulent flow as the Reynolds number increases are also clearly visible in Fig. 8. These smaller scales are visible in the leading-edge vortical system, the separated regions at both the wingtip and centerbody, and in the replacement of the largely laminar flow at the lower Reynolds numbers with the largely turbulent flow at $Re_{\text{mac}} = 59,758$ across much of the wing surface. Also, at all Reynolds numbers and angles of attack shown here, the presence of unsteady substructures in the leading-edge vortex are noted, similar to those observed in delta-wing simulations at both low-sweep [23] and high-sweep [47] configurations.

D. Examination of Averaged Flow Structure

To further elucidate the nature of the flow, the mean vortical structure on the leeward side of the UCAV was examined. Figure 9 highlights the vortical structure for the $\alpha = 6°$ case at the slightly different Reynolds number of $Re_{\text{mac}} = 32,000$ (this value corresponds to experimental data obtained in the Horizontal Free Water Tunnel Facility at Wright-Patterson Air Force Base [7] and was used to generate the images shown here [48].) At this angle of attack, a weak leading-edge vortex system is observed, with the primary vortex forming at the terminus of the separated leading-edge shear layer. Unlike previous simulation of canonical low-sweep delta wings [21], the leading-edge vortex does not form at the apex itself but at a location well downstream of the apex. Farther downstream, a dual-vortex system similar to that observed by Gordnier and Visbal [21] begins to form, due to the interaction of the primary shear layer with the secondary flow. This dual-vortex system is highlighted in Fig. 9b, with the primary and secondary vortices tracking in close proximity to each other as they travel downstream and finally weaken, due to the onset of unsteadiness near the wingtip. From Fig. 9c, the curved trajectory of the vortex system may be observed via the primary reattachment lines passing on the outboard side of the trailing-edge crank. Additional vortical structures may been seen inboard near the trailing edge of the wing, but these structures are small-scale in nature and are associated with the separation from the curved top surface of the vehicle.

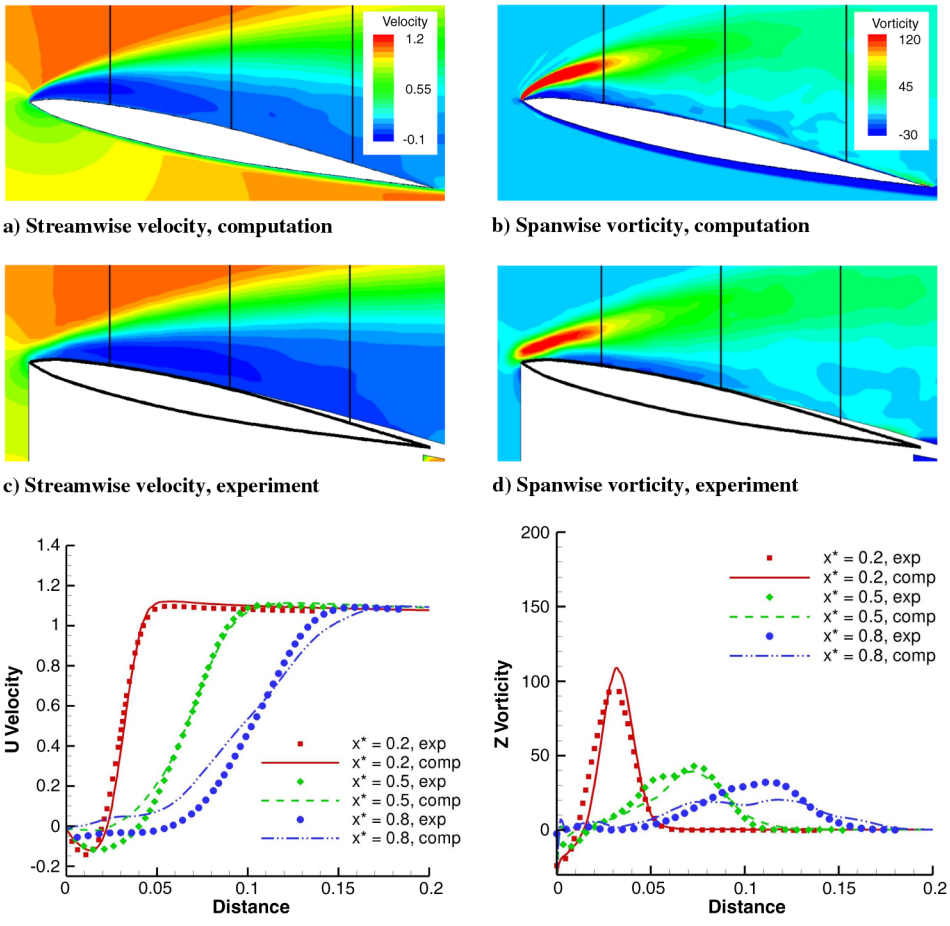

a) Streamwise velocity, computation

b) Spanwise vorticity, computation

c) Streamwise velocity, experiment

d) Spanwise vorticity, experiment

e) Quantitative comparison of computational and experimental data, streamwise velocity

f) Quantitative comparison of computational and experimental data, spanwise vorticity

Fig. 7 Comparison of mean streamwise velocity (left) and mean spanwise-normal vorticity (right) between computation and experiment at the spanwise station $\eta = 0.8$ for $\alpha = 12°$ and $Re_{\text{mac}} = 59,758$. Black vertical lines represent streamwise stations for quantitative comparisons.

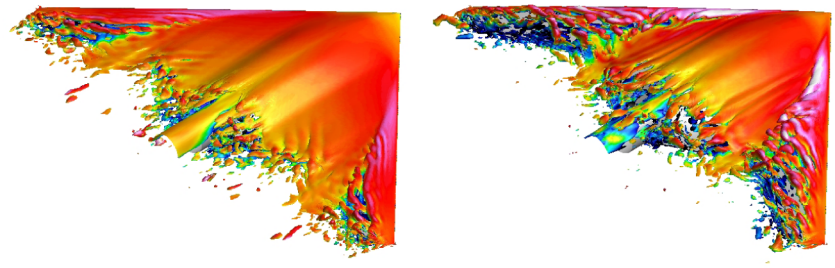

a) $\alpha = 6^{o}$, $Re_{mac} = 29879$ b) $\alpha = 12^{o}$, $Re_{mac} = 17927$

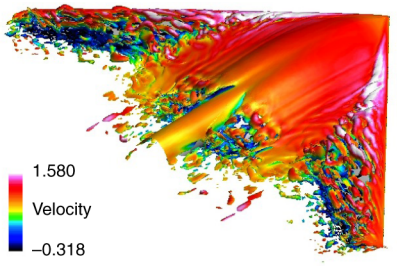

c) $\alpha = 12^{o}$, $Re_{mac} = 29879$

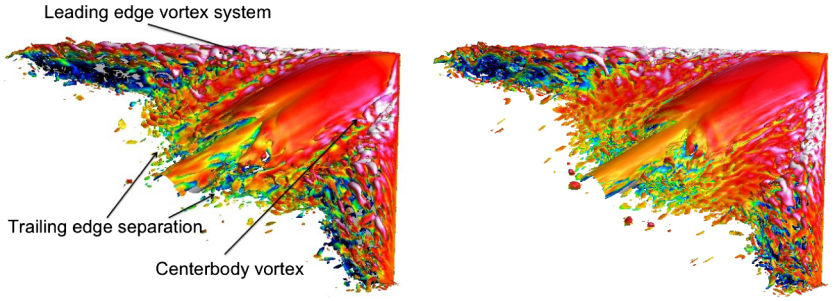

d) $\alpha = 15^{o}$, $Re_{mac} = 29879$ e) $\alpha = 12^{o}$, $Re_{mac} = 59758$

Fig. 8 Instantaneous isosurfaces of vorticity shaded by the streamwise velocity at various angles of attack and Reynolds numbers.

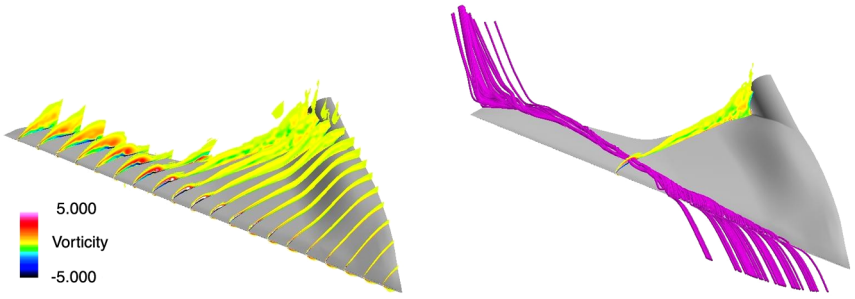

a) Mean axial vorticity at planes normal to leading edge

b) Off-body streamlines through main vortical structures

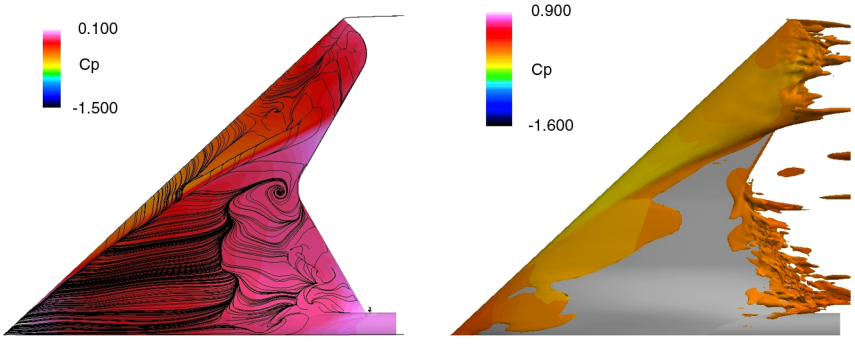

c) Surface streamlines superimposed over mean surface pressure distribution

d) Iso-surfaces of mean axial vorticity colored by pressure coefficient

Fig. 9 Flow features on leeward surface of 1303; $\alpha = 6°$ and $Re_{\mathrm{mac}} = 32,000$.

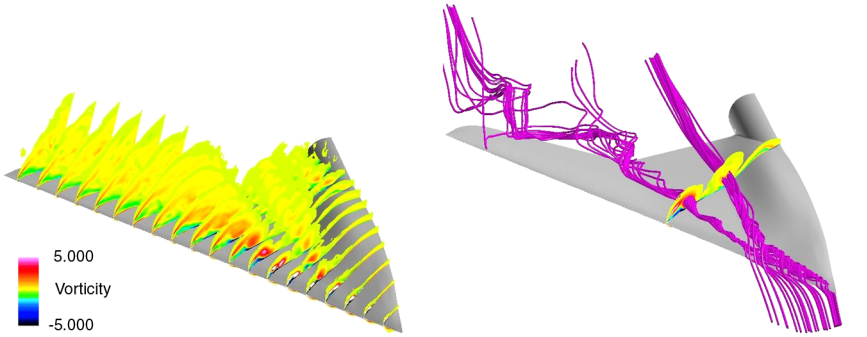

a) Mean axial vorticity at planes normal to leading edge

b) Off-body streamlines through main vortical structures

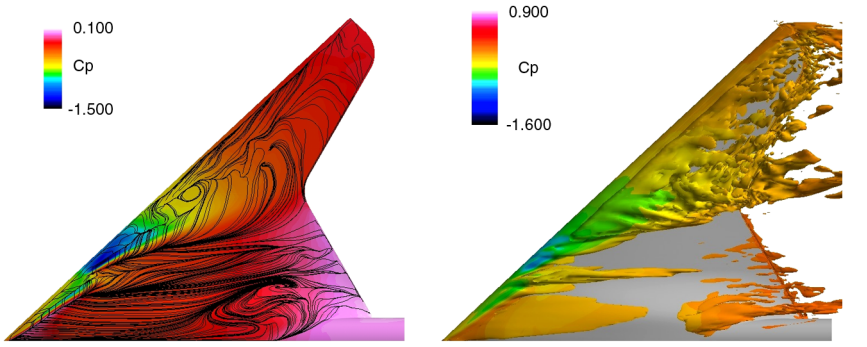

c) Surface streamlines superimposed over mean surface pressure distribution

d) Iso-surfaces of mean axial vorticity colored by pressure coefficient

Fig. 10 Flow features on leeward surface of 1303; $\alpha = 15°$ and $Re_{\text{mac}} = 32,000$.

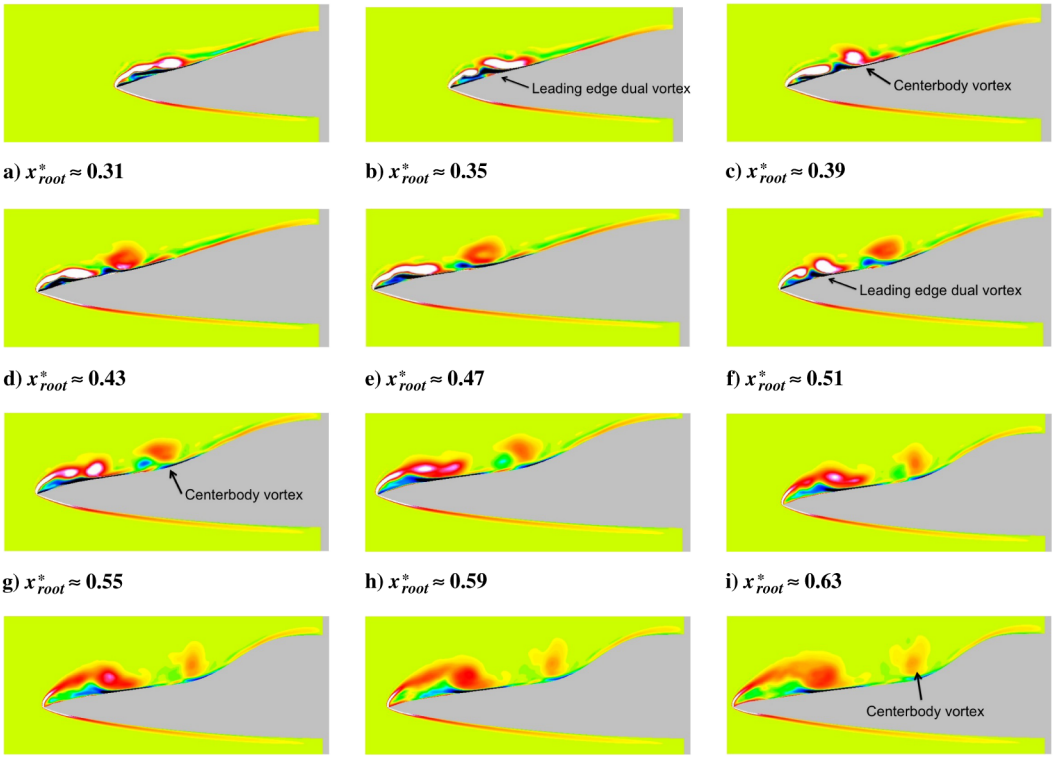

a) $x^*_{root} \approx 0.31$ b) $x^*_{root} \approx 0.35$ c) $x^*_{root} \approx 0.39$

d) $x^*_{root} \approx 0.43$ e) $x^*_{root} \approx 0.47$ f) $x^*_{root} \approx 0.51$

g) $x^*_{root} \approx 0.55$ h) $x^*_{root} \approx 0.59$ i) $x^*_{root} \approx 0.63$

j) $x^*_{root} \approx 0.67$ k) $x^*_{root} \approx 0.71$ l) $x^*_{root} \approx 0.75$

Fig. 11 Averaged axial vorticity contours at various streamwise planes, x^*_{root} is measured in nondimensional units from the apex, $\alpha = 15°$ (contours use the same legend as Fig. 10a).

At $\alpha = 15°$, a considerably different picture emerges, as demonstrated in Fig. 10. Here, a stronger and more complex vortical system emanates from the apex of the vehicle, but very quickly bifurcates into two distinct vortical structures. These structures appear to represent the "apex" vortex and the "wing" vortex that have previously been observed elsewhere in experiments at higher Reynolds numbers [4]. As both vortical structures have their origin in the unsteady shear layer emanating from the sharp leading edge, the vortex structures will be referred to here as the centerbody vortex for the inboard structure and the leading-edge vortex for the outboard structure. Both offbody and surface streamlines show the two vortex structures and their distinct trajectories. To further investigate the formation and behavior of these vortical structures, axial vorticity contours are presented in Fig. 11 at various nondimensional streamwise stations x^*_{root} across the geometry moving from the apex ($x^*_{\text{root}} = 0$) back toward the sting. In Figs. 11a–11c, the formation of the centerbody vortex is again due to the impingement of the surface secondary flow on the shear layer. However, because this process occurs close to the apex at this angle of attack, the newly formed vortex comes under the influence of the centerbody geometry and begins to follow a more streamwise trajectory, remaining in the juncture between the vehicle centerbody and the wing as it tracks downstream (Figs. 11d–11f). With no additional vorticity from the leading-edge shear layer to feed it, the centerbody vortex quickly loses strength and coherence as it travels downstream (Figs. 11g–11l).

Meanwhile, Figs. 11d–11f show the continued evolution of the leading-edge vortex system. The vortex formation process begins to repeat itself, whereby the secondary surface flow cuts the feeding vortex sheet of the shear layer. By $x^*_{\text{root}} = 0.51$, a new distinct leading-edge vortex structure is visible between the now weakening centerbody vortex and the feeding shear layer. However, this vortex is formed sufficiently far downstream and does not appear to come under the influence of the centerbody. Instead, it continues to interact with the vorticity from the unsteady shear layer and eventually recombines with the subsequent vortical structure at the terminus of the shear layer (Fig. 11h). The leading-edge vortex system then weakens and becomes less coherent as it moves downstream toward the wingtip (Figs. 11j–11l).

The trajectory of the leading-edge vortex system, best seen in the surface streamline patterns of Fig. 10c, follow a more curved trajectory than was observed in the $\alpha = 6°$ case (Fig. 9c) and pass over the wing just inboard of the trailing-edge crank. Additional coherent structure is also observed at the junction of the vehicle and the sting, indicating the formation of a vortex in this region.

Finally, the $\alpha = 12°$ case is considered in Fig. 12. At this angle of attack, the vortical structure appears to be of an intermediate nature between the relatively straightforward flow at $\alpha = 6°$ and the more complex flow at $\alpha = 15°$. At this angle of attack, there appears to be only one main vortical system associated with the leading edge of the wing. The trajectory of this vortical system falls in between the two previous angles of attack that were considered, with the vortex exiting the wing almost directly over the trailing-edge crank. While only one main vortical system is observed at the leading edge, its structure is considerably more complex than the dual-vortex system present at $\alpha = 6°$. The axial vorticity at various axial stations downstream of the apex is shown in Fig. 13. In Figs. 13a–13d, the process of vortex formation by cutting the feeding sheet is observed, and by $x^*_{\text{root}} = 0.51$, three distinct vortical structures may be discerned. However, this process takes place farther downstream than in the $\alpha = 15°$ case and thus farther from the influence of the centerbody geometry. Thus, the trajectory of the newly formed inboard vortex structure does not deviate far from the rest of the leading-edge vortical system and is rapidly dissipated. By $x^*_{\text{root}} = 0.71$ (Fig. 13g), the leading-edge system has reverted back to a dual-vortex structure as was seen in the $\alpha = 6°$ case, with the remnants of

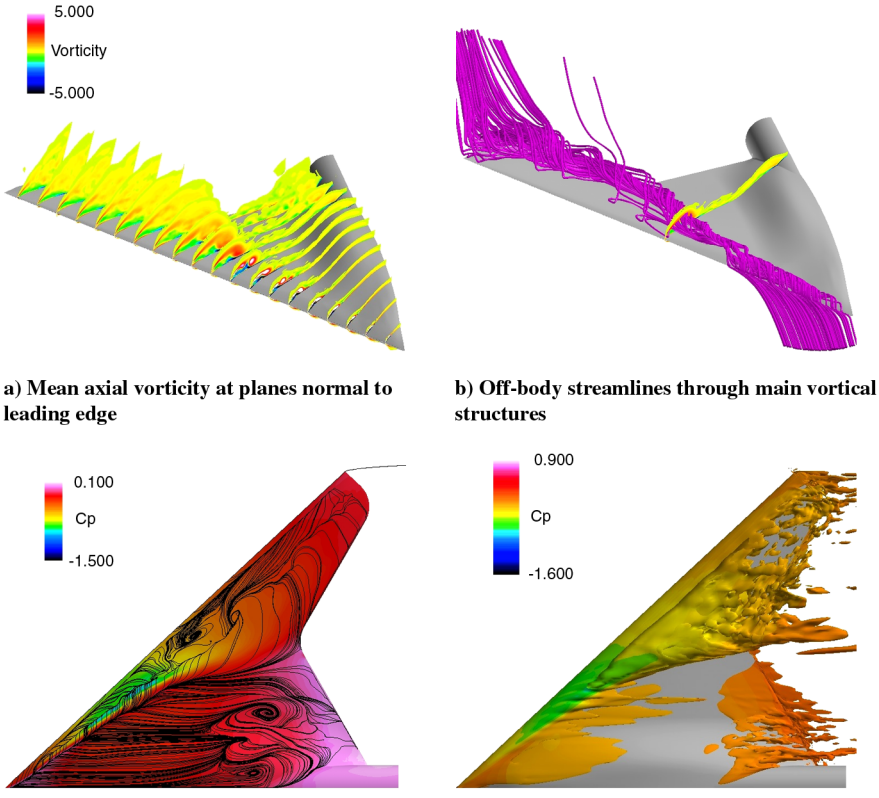

a) Mean axial vorticity at planes normal to leading edge

b) Off-body streamlines through main vortical structures

c) Surface streamlines superimposed over mean surface pressure distribution

d) Iso-surfaces of mean axial vorticity colored by pressure coefficient

Fig. 12 Vortical structure on leeward surface of 1303, $\alpha = 12°$ and $Re_{\text{mac}} = 32,000$.

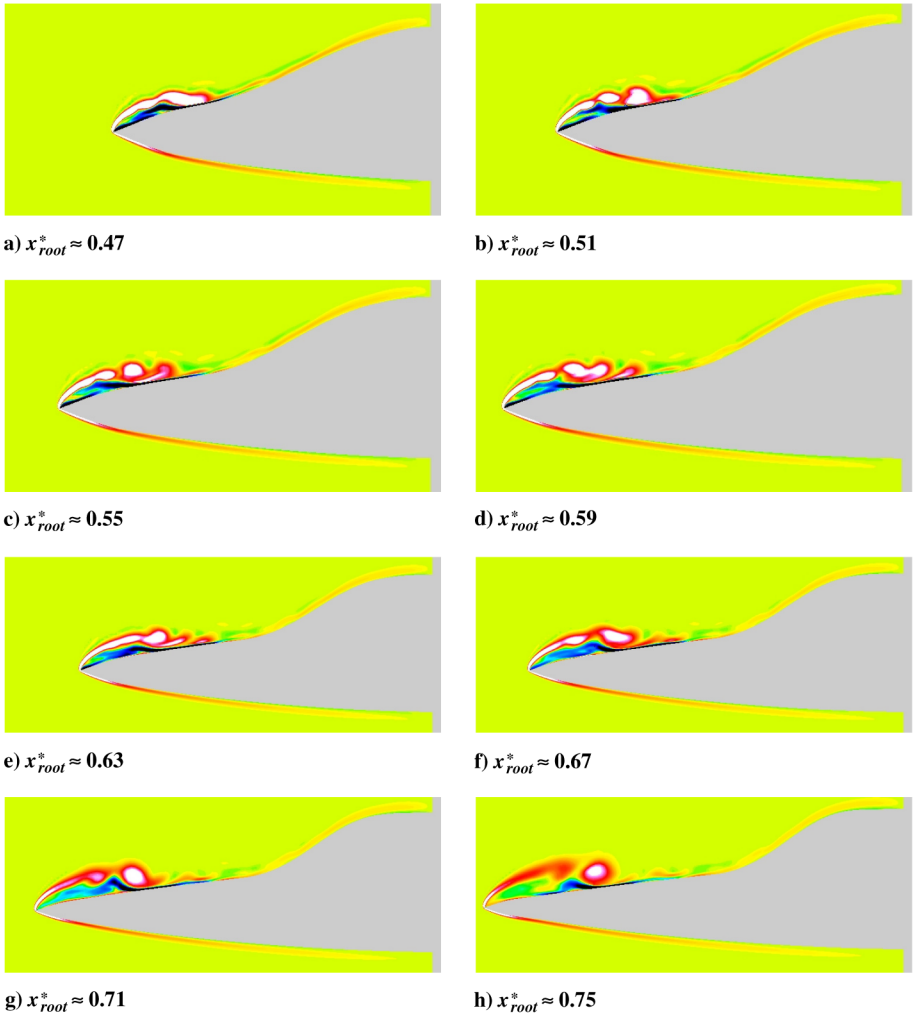

Fig. 13 Averaged axial vorticity contours at various streamwise planes, x^*_{root} is measured in nondimensional units from the apex, $\alpha = 12°$ (contours use the same legend as Fig. 12a).

the inboard vortex structure still visible. The leading-edge system then weakens and loses coherence as it moves downstream (Fig. 13h).

V. Conclusions

In this work, computations of the flowfield around a 1303 UCAV configuration with a sharp leading-edge geometry were performed using a high-order overset-grid algorithm. These computations were compared both quantitatively and qualitatively to recently collected PIV experimental data obtained in a free-surface water tunnel at various Reynolds numbers and angles of attack. Comparisons between computational and experimental results were quite good for most Reynolds numbers and angles of attack. The transitional nature of the flow and the impact of Reynolds number on the flowfield behavior demonstrates the flexibility of the implicit large-eddy simulation technique to seamlessly compute mixed laminar–turbulent flows. The formation and evolution of the leading-edge and centerbody vortical structures were also considered, and the impact of various angles of attack was examined. The 1303 UCAV represented a more realistic configuration than had been previously simulated with the high-order overset-grid solver, requiring overset constructs such as collar grids and wingtip grids to adequately resolve the geometry and providing a useful test case for the tools that have been developed to support high-order computations on more complex geometries. The development of such tools and their continuing maturation will allow the high-order algorithm to be employed more robustly on more elaborate overset topologies.

Acknowledgments

The computational work at the U.S. Air Force Research Laboratory (AFRL) was sponsored by the U.S. Office of Scientific Research (AFOSR) under a task monitored by John Schmisseur and Douglas Smith and supported in part by a grant of high-performance computing (HPC) time from the U.S. Department of Defence HPC Major Shared Resources Center at the AFRL. The experimental work at Lehigh University was sponsored by AFOSR grant FA9550-08-1-0022 monitored by John Schmisseur and Douglas Smith.

References

[1] Billman, G. M., and Osborne, B. A., "High L/D Extended Range/Payload Fighter Aircraft Technology," U.S. Air Force Research Lab., AFRL-VA-WP-TR-1999-3084, Air Vehicles Directorate, Nov. 1998.

[2] Bruce, R. J., "Low Speed Wind Tunnel Tests on the 1303 UCAV Concept," QinetiQ, Ltd., TR 025502, March 2003.

[3] McParlin, S. C., Bruce, R. J., Hepworth, A. G., and Rae, A. J., "Low Speed Wind Tunnel Tests on the 1303 UCAV concept," QinetiQ, Ltd., TR QinetiQ/fST/tR025502/1.0, March 2003.

[4] Ghee, T. A., "A Deployable Serrated Flap for Air Vehicle Control of a Representative UCAV Configuration," AIAA Paper 2002-3276, 2002.

[5] Ghee, T. A., "Parametric Evaluation of Deployable Serrated Flaps on a Representative UCAV Configuration," AIAA Paper 2003-3982, 2003.

[6] Ghee, T. A., and Hall, D. R., "Experimental and Numerical Investigation of Vortex Shedding of a Representative UCAV Configuration for Vortex Flow Control," RTO AVT Symposium, TR RTO-MP-069(I), Loen, Norway, May 2001.

[7] Ol, M. V., "Water Tunnel Velocimetry Results for the 1303 UCAV Configuration," AIAA Paper 2006-2990, 2006.

[8] Nelson, R., Corke, T., He, C., Othman, H., and Matsuno, T., "Modification of the Flow Structure Over a UAV Wing for Roll Control," AIAA Paper 2007-0884, 2007.
[9] Kosoglu, M., "Flow Structure Along a 1303 Unmanned Combat Air Vehicle," Ph.D. Thesis, Lehigh University, Bethlehem, PA, 2007.
[10] Wong, M. D., and Flores, J., "Application of OVERFLOW-MLP to the Analysis of the 1303 UCAV," AIAA Paper 2006-2987, 2006.
[11] Wong, M. D., McKenzie, G. J., OL, M. V., Petterson, K., and Zhang, S., "Joint TTCP CFD Studies into the 1303 UCAV Performance: First Year Results," AIAA Paper 2006-2984, 2006.
[12] Zhang, F., Khalid, M., and Ball, N., "A CFD Based Study of UCAV 1303 Model," AIAA Paper 2006-4615, 2005.
[13] Petterson, K., "CFD Analysis of the Low-Speed Aerodynamic Characteristics of a UCAV," AIAA Paper 2006-1259, 2006.
[14] Gursul, I., "Review of Unsteady Vortex Flows over Slender Delta Wings," *Journal of Aircraft*, Vol. 42, No. 2, March–April 2005, pp. 299–319.
doi:10.2514/1.5269
[15] Gursul, I., "Vortex Flows on UAVs: Issues and Challenges," *The Aeronautical Journal*, Vol. 108, No. 1090, Dec. 2004, pp. 597–610.
[16] Gursul, I., Gordnier, R., and Visbal, M., "Unsteady Aerodynamics of Nonslender Delta Wings," *Progress in Aerospace Sciences*, Vol. 41, 2005, pp. 515–557.
doi:10.1016/j.paerosci.2005.09.002
[17] Ol, M., and Gharib, M., "Leading-Edge Vortex Structure of Nonslender Delta Wings at Low Reynolds Number," *AIAA Journal*, Vol. 41, 2003, pp. 16–26.
doi:10.2514/2.1930
[18] Yavuz, M., Elkhoury, M., and Rockwell, D., "Near-Surface Topology and Flow Structure on a Delta Wing," *AIAA Journal*, Vol. 42, 2004, pp. 332–340.
doi:10.2514/1.3499
[19] Yaniktepe, B., and Rockwell, D., "Flow Structure on a Delta Wing of Low Sweep Angle," *AIAA Journal*, Vol. 42, 2004, pp. 513–523.
doi:10.2514/1.1207
[20] Yaniktepe, B., and Rockwell, D., "Flow Structure on Diamond and Lambda Planforms: Trailing-Edge Region," *AIAA Journal*, Vol. 43, 2005, pp. 1490–1512.
doi:10.2514/1.7618
[21] Gordnier, R. E., and Visbal, M. R., "Compact Difference Scheme Applied to Simulation of Low-Sweep Delta Wing Flow," *AIAA Journal*, Vol. 43, No. 8, 2005, pp. 1744–1752.
doi:10.2514/1.5403
[22] Gaitonde, D. V., and Visbal, M., "High-Order Schemes for Navier-Stokes Equations: Algorithm and Implementation into FDL3DI," U.S. Air Force Research Lab., AFRL-VA-WP-TR-1998-3060, Air Vehicles Directorate, Aug. 1998.
[23] Gordnier, R. E., and Visbal, M. R., "High-Order Simulation of Low Sweep Delta Wing Flows Using ILES and Hybrid RANS/ILES Models," AIAA Paper 2006-0504, 2006.
[24] Gordnier, R. E., Visbal, M. R., Gursul, I., and Wang, Z., "Computational and Experimental Investigation of a Nonslender Delta Wing," *AIAA Journal*, Vol. 47, No. 8, Aug. 2009, pp. 1811–1825.
doi:10.2514/1.37848
[25] Sherer, S. E., and Scott, J. N., "High-Order Compact Finite Difference Methods on General Overset Grids," *Journal of Computational Physics*, Vol. 210, No. 2, 2005, pp. 459–496.
doi:10.1016/j.jcp.2005.04.017
[26] Sherer, S. E., and Visbal, M. R., "Multi-Resolution Implicit Large Eddy Simulations Using a High-Order Overset-Grid Approach;," *International Journal for Numerical Methods in Fluids*, Vol. 55, 2007, pp. 455–482.
doi:10.1002/fld.1463
[27] Rizzetta, D. P., Visbal, M. R., Reed, H. L., and Saric, W. S., "Direct Numerical Simulation of Distributed Roughness on a Swept Wing Leading Edge," AIAA Paper 2010-377, 2010.
[28] Morgan, P. E., and Visbal, M. R., "Large Eddy Simulation of Flow over a Flat-Window Cylindrical Turret with Passive Flow Control," AIAA Paper 2010-916, 2010.
[29] Visbal, M. R., Morgan, P. E., and Rizzetta, D. P., "An Implicit LES Approach Based on High-Order Compact Differencing and Filtering Schemes," AIAA 16th Computational Fluid Dynamics Conf., AIAA Paper 2003-4098, Orlando FL, June 2003.
[30] Lele, S. K., "Compact Finite Difference Schemes with Spectral-like Resolution," *Journal of Computational Physics*, Vol. 103, 1992, pp. 16–42.
doi:10.1016/0021-9991(92)90324-R
[31] Gaitonde, D. V., and Visbal, M. R., "Padé-Type Higher-Order Boundary Filters for the Navier-Stokes Equations," *AIAA Journal*, Vol. 38, No. 11, 2000, pp. 2103–2112.
doi:10.2514/2.872
[32] Visbal, M. R., and Gaitonde, D. V., "High-Order-Accurate Methods for Complex Unsteady Subsonic Flows," *AIAA Journal*, Vol. 37, No. 10, 1999, pp. 1231–1239.
doi:10.2514/2.591
[33] Sherer, S., and Visbal, M., "Computational Study of Acoustic Scattering from Multiple Bodies Using a High-Order Overset Grid Approach," 9th AIAA/CEAS Aeroacoustics Conf., AIAA Paper 2003-3203, Hilton Head, SC, June 2003.
[34] Morgan, P., Visbal, M. R., and Rizzetta, D., "A Parallel High-Order Flow Solver for LES and DNS," AIAA 32nd Fluid Dynamics Meeting, AIAA Paper 2002-3123, St. Louis, MO, June 2002.
[35] Beam, R., and Warming, R., "An Implicit Factored Schemes for Compressible Navier-Stokes Equations," *AIAA Journal*, Vol. 16, No. 4, 1978, pp. 393–402.
doi:10.2514/3.60901
[36] Fyfe, D., "Economical Evaluation of Runge-Kutta Formulae," *Mathematics of Computation*, Vol. 20, 1966, pp. 392–398.
doi:10.1090/S0025-5718-1966-0202317-0
[37] Gordnier, R. E., and Visbal, M. R., "Numerical Simulation of Delta-Wing Roll," AIAA 31st Aerospace Sciences Meeting, AIAA Paper 93-0554, Reno, NV, Jan. 1993.
[38] Pulliam, T. H., and Chaussee, D., "A Diagonal Form of an Implicit Approximate-Factorization Algorithm," *Journal of Computational Physics*, Vol. 39, No. 2, 1981, pp. 347–363.
doi:10.1016/0021-9991(81)90156-X
[39] Suhs, N. E., Rogers, S. E., and Dietz, W. E., "PEGASUS 5: An Automated Pre-Processor for Overset-Grid CFD," AIAA 32nd Fluid Dynamics Meeting, AIAA Paper 2002-3186, St. Louis, MO, June 2002.
[40] Sherer, S. E., Visbal, M. R., and Galbraith, M. C., "Automated Preprocessing Tools for Use with a High-Order Overset-Grid Algorithm," AIAA Paper 2006-1147, 2006.
[41] Sherer, S. E., "Investigation of High-Order and Optimized Interpolation Methods with Implementation in a High-Order Overset Grid CFD Code," Ph.D. Thesis, Ohio State Univ., Columbus, OH, 2002.
[42] Benek, J., Steger, J., and Dougherty, F., "A Flexible Grid Embedding Technique with Application to the Euler Equations," AIAA Paper 83-1944, 1983.
[43] Sherer, S. E., "Further Analysis of High-Order Overset Grid Method with Applications," AIAA 16th Computational Fluid Dynamics Conf., AIAA Paper 2003-3839, Orlando, FL, June 2003.
[44] Yilmaz, T., and Rockwell, D., "Flow Structure on a Three-Dimensional Wing Subjected to Small Amplitude Perturbations," *Experiments in Fluids*., Vol. 47, Nos. 4–5, 2009, pp. 579–597.
doi:10.1007/s00348-009-0637-2
[45] Visbal, M. R., and Gaitonde, D. V., "Very High-Order Spatially Implicit Schemes for Computational Acoustics on Curvilinear Meshes," *Journal of Computational Acoustics*, Vol. 9, No. 4, 2001, pp. 1259–1286.
[46] Sherer, S. E., Visbal, M. R., and Gordnier, R. E., "Computational Study of Reynolds Number Effects on a 1303 UCAV Configuration with a High-Order Overset-Grid Algorithm," AIAA 47th Aerospace Sciences Meeting, AIAA Paper 2009-751, Orlando, FL, Jan. 2009.
[47] Visbal, M. R., and Gordnier, R. E., "On the Structure of the Shear Layer Emanating from a Swept Leading Edge at Angle of Attack," AIAA Paper 2003-4016, 2003.
[48] Sherer, S. E., Visbal, M. R., and Gordnier, R. E., "Computational Study of a UCAV Configuration Using a High-Order Overset-Grid Algorithm," AIAA 46th Aerospace Sciences Meeting, AIAA Paper 2008-626, Reno, NV, Jan. 2008.